



Published in final edited form as:

*J Phys Chem Lett.* 2019 April 18; 10(8): 1644–1652. doi:10.1021/acs.jpcclett.9b00099.

## Complete Phase Diagram for Liquid–Liquid Phase Separation of Intrinsically Disordered Proteins

James McCarty<sup>†,‡</sup>, Kris T. Delaney<sup>‡</sup>, Scott P. O. Danielsen<sup>‡,¶</sup>, Glenn H. Fredrickson<sup>‡,¶,§</sup>,  
Joan-Emma Shea<sup>†,‡,||</sup>

<sup>†</sup>Department of Chemistry and Biochemistry, University of California, Santa Barbara, California 93106, United States

<sup>‡</sup>Materials Research Laboratory, University of California, Santa Barbara, California 93106, United States

<sup>¶</sup>Department of Chemical Engineering, University of California, Santa Barbara, California 93106, United States

<sup>§</sup>Materials Department, University of California, Santa Barbara, California 93106, United States

<sup>||</sup>Department of Physics, University of California Santa Barbara, Santa Barbara, California 93106, United States

### Abstract

A number of intrinsically disordered proteins have been shown to self-assemble via liquid–liquid phase separation into protein-rich and dilute phases. The resulting coacervates can have important biological functions, and the ability to form these assemblies is dictated by the protein's primary amino acid sequence as well as by the solution conditions. We present a complete phase diagram for the simple coacervation of a polyampholyte intrinsically disordered protein using a field-theoretic simulation approach. We show that differences in the primary amino acid sequence and in the distribution of charged amino acids along the sequence lead to differences in the phase window for coacervation, with block-charged sequences having a larger coacervation window than sequences with a random patterning of charges. The model also captures how changing solution conditions modifies the phase diagram and can serve to guide experimental studies.

### Graphical Abstract

---

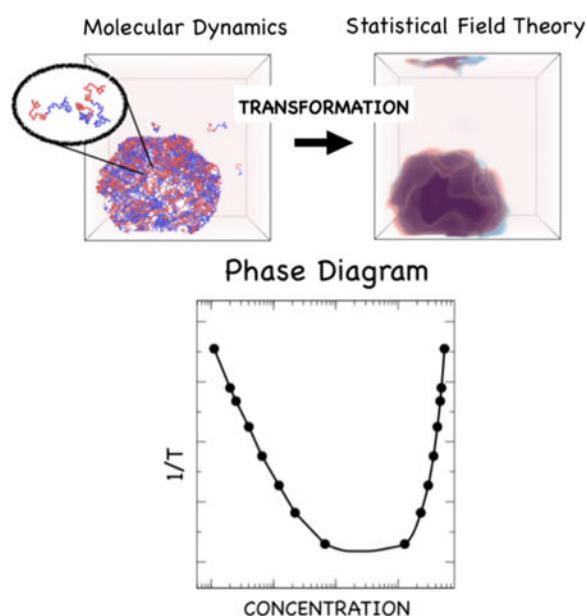
#### ASSOCIATED CONTENT

##### Supporting Information

The Supporting Information is available free of charge on the ACS Publications website at DOI: [10.1021/acs.jpcclett.9b00099](https://doi.org/10.1021/acs.jpcclett.9b00099).

Details of the field-theoretic simulation (FTS) procedure and methods, a definition of the operators used in FTS to evaluate thermodynamic quantities, details of the particle molecular dynamics (MD) simulations, treatment of long-range electrostatics in the MD simulations, the RPA for the polyelectrolyte model, the Gibb's ensemble method to compute phase coexistence points for phase diagrams, extension of the polymer field theory Hamiltonian to include explicit salt ions, and a comparison of the structure factors among MD, FTS, and RPA (PDF)

The authors declare no competing financial interest.



Intrinsically disordered proteins (IDP), unlike globular proteins, do not fold to a well-defined folded three-dimensional structure but rather populate a variety of partially structured, marginally stable conformations under physiological conditions. IDPs play a variety of roles in the cell, from cell signaling to transduction, functions that take advantage of the IDPs' ability to adopt structures that can bind to different partners.<sup>1–3</sup> The lack of a well-folded structure with a buried hydrophobic core heightens the likelihood that these structures will aggregate in a concentrated cellular environment. A well-characterized aggregated form of IDPs is the amyloid fibril, a solid entity with an ordered cross- $\beta$ -sheet structure that deposits on organs in the body and is a hallmark of amyloid diseases.<sup>4,5</sup> A growing number of IDPs have also been observed to undergo a different form of assembly process, a liquid–liquid phase separation (LLPS) known as coacervation, which manifests as the formation of protein-rich liquid droplets of biomolecular aggregates.<sup>6–11</sup> The process of coacervation has been observed in proteins associated with amyloid diseases (for example, the tau protein implicated in tauopathies,<sup>10</sup> and the FUS protein linked to ALS<sup>8</sup>), which has led to speculation that liquid droplet formation might play a role in the IDP fibrillization process.<sup>12–14</sup> It remains unclear whether the droplets are on-pathway to fibril formation, maturing from a liquid state to a solid state, or whether the droplets rather sequester peptides and offer an alternate to fibrillization. In some instances, the role of the liquid droplets appears to be purely physiological, forming membrane-less organelles such as the Cajal and nuclear bodies, storing peptides, or serving as reactive centers in which biomolecular reactions can proceed at an accelerated rate.<sup>6,11,15,16</sup>

While it is recognized that the unique amino acid sequence for a given IDP ultimately determines the phase behavior, few theories are able to model polyampholyte coacervation for heterogeneous polymers such as IDPs.<sup>17</sup> In IDPs, as opposed to synthetic polyelectrolytes, the placement of charges along the chain is not random, and one expects correlations among charges introduced by chain connectivity to play an important role in controlling the phase behavior. However, these intramolecular charge correlations are

neglected by mean-field approaches such as the widely used Voorn–Overbeek (VO) model.<sup>18,19</sup> Recent theoretical work has called attention to the fact that the simple VO model neglects this important physics, leading to incorrect scaling predictions over all concentration ranges.<sup>20</sup> If a polymer physics model is to be applied to IDPs, it must properly account for heterogeneous sequences and make predictions based on the specific charge distribution of a given IDP. Explicit charge patterning was introduced in a recently proposed theoretical model<sup>21,22</sup> based on the random phase approximation (RPA),<sup>23</sup> demonstrating that the pattern of charges has a large effect on the phase diagram.<sup>24</sup> The RPA model is a marked improvement over mean-field approaches and can be formally derived by considering Gaussian fluctuations in the fields.<sup>25</sup> Despite its qualitative success, the RPA is expected to break down under conditions at which field fluctuations become large. For example, Monte Carlo simulations of lattice chains have shown that the RPA model overpredicts the dependence of charge sequence on the stability of the homogeneous phase.<sup>26</sup> Recent theoretical efforts have aimed at a more sophisticated treatment of fluctuations and electrostatic correlations through either a renormalization approach<sup>27,28</sup> or a hybrid approach in which theory is informed from simulation.<sup>29–31</sup>

Complementary to analytical theories are numerical methods, such as molecular dynamics (MD) simulation. All-atom explicit-water MD is useful to study the early stages of aggregation in short chains but is computationally expensive, which hinders its applicability for studying IDP phase separation. On the other hand, coarse-grained models are useful for understanding how the parametrization of the potential of mean force acting between effective segments of the polyampholyte model can affect the phase diagram.<sup>32</sup> For example, an approach using a slab geometry developed for vapor–liquid transitions<sup>33,34</sup> has recently been introduced to achieve a converged density profile within a coarse-grained MD simulation, enabling computation of the phase diagram.<sup>32,35</sup> Still, these methods require long equilibration times to obtain the phase coexistence points and suffer from finite size effects due to the limited number of chains that can be reasonably included in the simulation box.

An alternative to these theoretical and particle-based approaches is to employ field-theoretic simulation (FTS),<sup>36,37</sup> which is a numerical technique based on the formal equivalence between a particle-based representation and a statistical field description in which ensemble averages are evaluated as path integrals over spatially varying chemical and electrostatic potential field configurations. A major advantage of FTS over other methods such as self-consistent field theory or the RPA is that FTS stochastically samples the fully fluctuating field-theoretic Hamiltonian, making it possible to generate phase diagrams without additional approximations. In the context of IDP phase separation, FTS is appealing because one can efficiently simulate large dense systems without invoking uncontrolled approximations, as done in the RPA, and without the need for long equilibration times, as required by particle-based MD. This method has been applied to study polyelectrolyte coacervation for relatively simple homopolymers and block copolymers.<sup>20,38–40</sup> We introduce in this Letter a discrete-chain implementation to study the effect of sequence variation at the individual monomer level, a critical feature in order to describe IDP coacervation. IDP coacervation can occur in a simple or complex manner (the latter requiring the presence of a second type of molecule, typically RNA), but we focus here on

simple coacervation, noting that the methodology presented can be readily extended to complex coacervation. IDPs come in a variety of flavors, and we study in this Letter the archetypal liquid–liquid phase-separating IDP, a polyelectrolyte consisting of the same number of positively charged and negatively charged monomers. Electrostatic effects on the phase diagram emerge not just as a result of the net charge or charge density but also on how the individual charged residues are arranged along the chain into charged “patches”. Clustering of like charges into a local charge patch amplifies their effect, whereas scattering charges diminishes their effect due to screening from proximal oppositely charged residues. 11,24,41,42

To study the role of charge–charge interactions in driving self-coacervation, we consider different permutations of positively and negatively charged monomers based on the sequences of 25 lysine (K) and 25 glutamic acid (E) residues introduced by Das and Pappu.<sup>41</sup> The five sequences considered exhibiting different patterning of E and K are shown in Figure 1. Because FTS fully samples compositional fluctuations, we are able to efficiently compute both dilute and concentrated regimes and to present a complete phase diagram for the coacervation of model IDP sequences with different distributions of charged residues. We also introduce particle-based MD simulations to expose the individual-chain structures in the dilute states and to provide an additional consistency check of our FTS results. A detailed comparison of the structural correlations within the solution phase for the various EK sequences is presented in the Supporting Information.

Our system consists of  $n$  polymers with  $N$  monomers per chain in a volume  $V$ , with a resulting monomer number density  $\rho = nN/V$ . Each monomer has a site-specific charge in units of the electronic charge  $e$  such that each chain  $\alpha$  has a charge pattern  $\{\sigma_{\alpha,j}\} = \{\sigma_{\alpha,1}, \sigma_{\alpha,2}, \dots, \sigma_{\alpha,N}\}$ , where  $\sigma_{\alpha,j}$  is the charge of the  $j$ th residue on chain  $\alpha$ . Chain connectivity is enforced by a harmonic bond potential  $\beta U_{\text{bond}} = \frac{3}{2b^2} \sum_{\alpha=1}^n \sum_{j=1}^N (|\mathbf{r}_{\alpha,j} - \mathbf{r}_{\alpha,j-1}|)^2$  where  $\mathbf{r}_{\alpha,j}$  denotes the position of bead  $j$  on chain  $\alpha$ ,  $b$  is the statistical segment length, and  $\beta = 1/k_B T$ . The solvent is treated implicitly as a uniform dielectric continuum. All monomers interact through an excluded volume potential  $\beta U_{\text{ex}} = v\delta(\mathbf{r})$ , where  $v$  is the excluded volume parameter, taken to be identical for all monomer types.<sup>44,45</sup> Electrostatic interactions are described by a Coulomb potential  $\beta U_{\text{el}} = \frac{l_B \sigma_i \sigma_j}{r}$ , where  $l_B = e^2/(4\pi\epsilon_0\epsilon_r k_B T)$  is the Bjerrum length,  $\epsilon_0$  is the vacuum permittivity,  $\epsilon_r$  is the relative dielectric strength of the solvent, and  $e$  is the unit of electronic charge. The total microscopic bead number density is  $\hat{\rho}(\mathbf{r}) = \sum_{\alpha}^n \sum_j^N \delta(\mathbf{r} - \mathbf{r}_{\alpha,j})$ , and similarly, the total microscopic charge density is  $\hat{\rho}_e(\mathbf{r}) = \sum_{\alpha}^n \sum_j^N \sigma_{\alpha,j} \delta(\mathbf{r} - \mathbf{r}_{\alpha,j})$ . These microscopic densities are smeared so that both masses and charges have a Gaussian distribution.<sup>20,46</sup> The smeared densities corresponding to either  $\hat{\rho}(\mathbf{r})$  or  $\hat{\rho}_e(\mathbf{r})$  are

$$\bar{\rho}(\mathbf{r}) = \int d\mathbf{r}' \Gamma(|\mathbf{r} - \mathbf{r}'|) \hat{\rho}(\mathbf{r}') \quad (1)$$

with

$$\Gamma(r) = \left(\frac{1}{2\pi a^2}\right)^{3/2} \exp(-r^2/2a^2) \quad (2)$$

a normalized Gaussian with smearing width  $a$ . The resulting interaction energy for this model is

$$\begin{aligned} \beta\bar{U}[\mathbf{r}] = & \frac{3}{2b^2} \sum_{\alpha=1}^n \sum_{j=1}^N (|\mathbf{r}_{\alpha,j} - \mathbf{r}_{\alpha,j-1}|)^2 + \frac{v}{2} \int d\mathbf{r} \bar{\rho}^2(\mathbf{r}) \\ & + \frac{l_B}{2} \iint d\mathbf{r} d\mathbf{r}' \frac{\bar{\rho}_e(\mathbf{r})\bar{\rho}_e(\mathbf{r}')}{|\mathbf{r} - \mathbf{r}'|} \end{aligned} \quad (3)$$

The essential features of the model are chain connectivity (first term), short-ranged excluded volume repulsion (second term), and long-ranged electrostatic interactions (third term). A major effort of this work is to delineate how differences in the charge pattern  $\{\sigma_{\alpha,j}\}$  affect the structural and thermodynamic properties of this model. To accomplish this, we take advantage of an exact transformation of this model into a statistical field theory.

Following the method described in ref 25, the canonical partition function for the model Hamiltonian given by eq 3 can be expressed as a complex-valued statistical field theory

$$\mathcal{Z}_c = \mathcal{Z}_0 \int Dw \int D\varphi e^{-H[w,\varphi]} \quad (4)$$

where  $\mathcal{Z}_0$  is the partition function for an ideal gas of discrete Gaussian chains and self-interaction correction terms. An extension of the model to include small ions explicitly is described in the Supporting Information. The field-theoretic Hamiltonian is

$$\begin{aligned} H[w,\varphi] = & \frac{1}{2} \int d\mathbf{r} \left( \frac{[w(\mathbf{r})]^2}{v} + \frac{[\nabla\varphi(\mathbf{r})]^2}{4\pi l_B} \right) \\ & - n \ln Q[w,\varphi] \end{aligned} \quad (5)$$

where  $w$  is a fluctuating chemical potential field and  $\varphi$  is a fluctuating electrostatic potential field, which serve to decouple pairwise interactions.  $Q[w,\varphi]$  is the partition function for a single chain in a complex-valued external field and can be computed using a Gaussian chain propagator

$$Q[w,\varphi] = \frac{1}{V} \int d\mathbf{r} q_N(\mathbf{r}; [w,\varphi]) \quad (6)$$

The chain propagator  $q_N(\mathbf{r}; \psi)$  can be constructed from the following Chapman–Kolmogorov-type equation

$$q_{j+1}(\mathbf{r}; \psi) = \left(\frac{3}{2\pi b^2}\right)^{3/2} \exp[-\psi_{j+1}(\mathbf{r})] \int d\mathbf{r}' q_j(\mathbf{r}'; \psi) \exp\left(-\frac{3|\mathbf{r} - \mathbf{r}'|^2}{2b^2}\right) \quad (7)$$

with  $\psi_j = i\Gamma \star (w + \sigma_j \varphi)$ , where  $i = \sqrt{-1}$  and  $\star$  denotes a spatial convolution. The initial condition is  $q_0(\mathbf{r}; [\psi]) = \exp[-\psi_0(\mathbf{r})]$ .

As described elsewhere,<sup>20,46</sup> FTSs are performed using complex Langevin (CL) sampling of the fields. After promoting the fields to be complex variables, the CL equations of motion are

$$\begin{aligned} \frac{\partial w(\mathbf{r}, t)}{\partial t} &= -\lambda_w \frac{\delta H(w, \varphi)}{\delta w(\mathbf{r}, t)} + \eta_w(\mathbf{r}, t) \\ \frac{\partial \varphi(\mathbf{r}, t)}{\partial t} &= -\lambda_\varphi \frac{\delta H(w, \varphi)}{\delta \varphi(\mathbf{r}, t)} + \eta_\varphi(\mathbf{r}, t) \end{aligned} \quad (8)$$

where  $\eta(\mathbf{r}, t)$  are real-valued Gaussian white noise random variables with zero mean and variance proportional to the dissipative coefficients  $\lambda_w$  and  $\lambda_\varphi$ . By propagating the CL equation of motion in time, FTS stochastically samples the configuration space of the conjugate field variables. Details of the CL-FTS procedure are presented in the Supporting Information.

For use in conventional MD simulation of bead–spring chains, we present an equivalent particle-based representation for a system with potential energy given by eq 3. This amounts to expressing each of the interactions in eq 3 as effective pair potentials. The bond potential between beads separated by distance  $r$  is

$$\beta V_{\text{bond}}(r) = \frac{3}{2b^2} r^2 \quad (9)$$

The smeared Gaussian densities of eq 3 can be equivalently treated as point particles interacting through a soft potential, finite at contact. In this representation, the excluded volume interaction between monomers is equivalent to an effective soft Gaussian repulsive interaction of the form

$$\beta U_{\text{ev}}(r) = \frac{v}{8\pi^{3/2} a^3} e^{-r^2/4a^2} \quad (10)$$

and the electrostatic potential is similarly<sup>47,48</sup>

$$\beta U_{\text{el}}(r) = \frac{l_B \sigma_i \sigma_j}{r} \text{erf}\left(\frac{r}{2a}\right) \quad (11)$$

Particle simulations were carried out using the LAMMPS MD code<sup>49</sup> (<http://lammmps.sandia.gov>). Details of the simulation procedure are presented in the Supporting Information. It is important to note that both MD and FTS are here performed on the same

polymer model. While the FTS and MD simulations numerically sample the full Hamiltonian, it also proves instructive to consider the RPA approximation for this model, which provides an analytical approximation that we compare directly to FTS simulation and discuss the limits of its validity. Details of the derivation of the RPA expressions are given in the Supporting Information.

The equilibrium conditions for the phase coexistence between a dense coacervate phase and a dilute solution phase are the equivalence in osmotic pressure  $\Pi$  and chemical potential  $\mu$  of the two phases. Before investigating the phase diagram, it is instructive to compare these thermodynamic observables computed from FTS, MD, and RPA. A plot of the osmotic pressure  $\Pi$  as a function of the monomer density at fixed temperature gives the numerical equation of state. Figure 2 (left column) presents a comparison among FTS (square), RPA (line), and particle MD (circle) of the excess osmotic pressure for two representative chains *sv20* (Figure 2A) and *sv30* (Figure 2B). Results are presented for two values of the Bjerrum length  $l_B$ , which parametrizes the strength of the electrostatic potential in eq 3. Increasing  $l_B$  by an order of magnitude from a relatively weak value  $l_B = 0.033b$  (black) to a more modest  $l_B = 0.33b$  (red) has the effect of lowering the osmotic pressure curve due to the increased strength of favorable electrostatic attractions between oppositely charged monomers. This effect is more pronounced in the diblock *sv30* sequence. For these parameter ranges, the analytical RPA approximation is in agreement with FTS. Particle MD simulations become increasingly difficult to equilibrate at high polymer densities but agree with both FTS and RPA at low and intermediate densities.

Figure 2 (right column) compares the chemical potential between the analytical RPA prediction (line) and the exact value from FTS (square) for chain *sv20* (Figure 2C) and *sv30* (Figure 2D). (Note that direct computation of the chemical potential with MD simulations is not shown as the calculation requires either thermodynamic integration or a Widom insertion method.) Importantly, while accurate for large monomer densities, the RPA approximation breaks down at low density. The difference between FTS and RPA becomes more pronounced at higher values of  $l_B$ . Figure 2 demonstrates that particle MD simulations are suitable for low to intermediate densities, whereas the RPA is valid at high densities. This observation motivates the use of FTS as a method to study phase behavior as it is capable of accurately describing the thermodynamics over the entire density range of interest. Although it is possible to use particle-based MD simulations to compute phase diagrams using the method described in refs 32 and 35, this requires equilibrating a MD simulation at each state point of interest and is not pursued here as it is computationally expensive. The purpose of this Letter is to demonstrate the applicability of FTS to efficiently compute phase diagrams that accurately capture both the dilute and concentrated branches.

As discussed above, the Bjerrum length  $l_B$  controls the strength of the electrostatic potential. Increasing  $l_B$  leads to an increasing density fluctuation length scale, implying an approaching critical point (see the Supporting Information). The magnitude of the Bjerrum length in this work is chosen to expose the critical region of the phase diagram for these model peptides. For water at 300 K, the Bjerrum length is typically on the order of  $b$ ; however, the model peptides examined here have a much higher charge density than typical proteins and thus phase separate at lower values of the Bjerrum length.

Performing FTS in the Gibbs ensemble<sup>50,51</sup> is an efficient way to construct the exact binodal curve for all five of the sequences shown in Figure 1 as a function of the reduced Bjerrum length  $l_B/b$ . Details of the Gibbs ensemble procedure are presented in the Supporting Information. The coexistence points determined from FTS in the Gibbs ensemble provide an efficient enumeration of the phase diagram for an IDP described by eq 3 without introducing additional approximations. At low density, the dilute solution phase is favored. Increasing the protein concentration through  $\rho b^3$  leads to a two-phase region in which both the solution and coacervate phase are in coexistence (with concentrations shown by the data points). At sufficiently high protein concentration, only a dense coacervate phase is stable. A snapshot of the density profile of each of these regions from FTS is presented in the top panel of Figure 3A.

The exact phase diagram for this coarse-grained model, fully accounting for compositional fluctuations, for the five model sequences is shown in Figure 3B,C and is compared with the RPA approximation. The Bjerrum length can be used to define a reduced temperature  $T^* = b/l_B = 4\pi\epsilon_0\epsilon_r k_B T b / e^2$ . Thus, Figure 3B is analogous to an experimental inverse temperature vs concentration plot. For comparison, Figure 3C shows the same data plotted as a reduced temperature vs monomer density. Both RPA and FTS show that by sequestering charges into larger “patches” the critical Bjerrum length for phase separation is lowered. Although the RPA model qualitatively describes the sequence-dependent critical point, the low-density branch of the binodal is incorrect. The reason for the failure of the RPA at low concentration is largely due to the estimation of the chemical potential at low density, as seen in Figure 2. Nonetheless, the RPA prediction is qualitatively correct at modeling the sequence dependence and becomes quantitative at sufficiently high densities. This finding is in agreement with Lin and Chan who used the RPA model to study these same sequences in ref 24. We note that the linear density scale in Figure 3C conceals this difference between FTS and RPA for the dilute branch.

In dilute polymer solutions, electrostatic effects can lead to single-chain compaction or swelling.<sup>52–54</sup> At high enough polymer densities, it has been argued that these same electrostatic effects lead to interpolymer associations, driving phase separation.<sup>24,55–57</sup> To investigate this, we performed particle MD simulations of single chains in implicit solvent. Figure 4A shows that larger charge “patches” of oppositely charged residues along the same chain result in a lower average radius of gyration  $R_g$  due to electrostatic attraction. The lower  $R_g$  is due to the chain sampling fewer extended configurations. The observed dependence of  $R_g$  on the charge patterning shown in Figure 4A is in qualitative agreement with results from coarse-grained simulations presented by Das and Pappu;<sup>41</sup> however, those simulations used a hard repulsive potential instead of the soft Gaussian potential employed here, which allows the chains to become more compact in the present work. Figure 4B shows an example of the compact configuration for the diblock chain (sv30), and Figure 4C shows a similar snapshot of two chains taken from a simulation of 300 chains in the early stages of IDP aggregation. These snapshots suggest that similar electrostatic effects control single-chain compactness and multiple-chain aggregation.

Figure 4 implies that under dilute conditions the Gaussian form factors used in the RPA approximation are not physically realistic and may be partially responsible for the



breakdown of the RPA at dilute concentrations. Using the numerical form factor from short MD simulations could potentially improve the RPA prediction. Such an approach would be similar in spirit to the recent Gaussian renormalization model, which introduced a self-consistent single-chain structure to improve the RPA prediction for homopolyelectrolytes.<sup>27</sup>

Thus far, we have focused exclusively on varying the Bjerrum length  $l_B$ . In our model, two other factors control the phase behavior, namely, the strength of the excluded volume parametrized by  $\nu$  in eq 3 and the concentration of excess salt, which is expected to screen electrostatic interactions. The excluded volume is a nonelectrostatic interaction parameter that describes the solvent quality with a temperature dependence typically of the form  $\nu = \nu_0(1 - \theta/T)$ , where  $\nu_0$  controls the strength of the interaction and  $\theta$  is a protein-specific reference temperature. It should be noted that for largely hydrophobic sequences, instead of the charged sequences considered in this work, the temperature dependence of  $\nu$  may be more complex. Figure 5A shows the binodal coexistence points as a function of  $\nu$  for four of the five sequences at a fixed value of  $l_B = 0.33b$ . Note that at this value of  $l_B$  the most charge-scrambled sequence *sv10* is in the solution phase for all values of  $\nu$  and is not shown. It can be seen that increasing the excluded volume strength  $\nu$ , i.e., increasing the solvent quality, tends to stabilize the mixed phase and prevent phase separation, in agreement with the theoretical work of Perry and Sing<sup>58</sup> on model synthetic polyelectrolytes. This is due to an increase in the repulsive interaction between monomer segments that counteracts the electrostatic attraction between oppositely charged segments.

Figure 5B shows a similar suppression of the two-phase window by added salt. Explicit salt ions are introduced as point charges with microscopic density smeared with a normalized Gaussian profile. The field-theoretic Hamiltonian with explicit salts is presented in the Supporting Information. For simplicity, the smearing length is the same for both salt and monomers; however, one could adopt different smearing lengths to model different salt ion sizes. The observed trend in Figure 5B with salt is in qualitative agreement with experimental observations of simplified systems and real IDPs. A more detailed discussion of the effect of salt is the subject of a forthcoming paper.<sup>59</sup>

In this Letter, we have introduced a polyampholyte model to describe IDPs and have demonstrated the applicability of FTS to study how the spatial organization of amino acids can mediate IDP phase behavior. The polyampholyte model that we have considered represents the simplest coarse-grained model that still captures the relevant physical features of the problem. While in this work we have selectively focused on the clustering of charged amino acids and therefore have considered a low-complexity sequence of just two amino acids (E and K), the model can be generalized to introduce additional nonelectrostatic interactions such as hydrophobic or  $\pi$ -stacking interactions. Using FTS, we construct an exact phase diagram for this model in terms of the dielectric strength, polymer excluded volume (solvent quality), and salt concentration. Our results show that clustering of charged amino acids into charged patches significantly modulates the phase diagram, in agreement with experiments performed on sequence variants of the germ-granule protein Ddx4.<sup>60</sup>

Direct comparison among particle MD simulation, FTS, and RPA theory for the same polyelectrolyte model allows us to comment on the limitations and merits of these different

approaches. Because particle MD simulation provides structural information about single-chain configurations, it can be useful to test predictions of intramolecular form factors and chain configurational distributions. It also offers site-specific resolution of chain associations as well as information about dynamics. However, MD simulation requires exceedingly long equilibration times for dense phase-separating systems and is thus limited to the regime of relatively low polymer density. On the other hand, analytical RPA theory is valid only at sufficiently high polymer densities, in agreement with previous observations.<sup>20,38,39</sup> This implies that one should be cautious about fitting the RPA model to the low-density branch of an experimental phase diagram. Despite its quantitative limitations compared to FTS, the RPA qualitatively captures the effect of charge sequence variation on the phase diagram, validating the recent application of the RPA model for these sequences.<sup>21,24</sup> By providing an exact numerical result, FTS is a useful technique against which RPA or other more advanced theories may be tested.

In summary, this Letter presents a general framework from which to study LLPS in biology. By considering a model system of low sequence-complexity peptides, we have demonstrated the ability of FTS to generate complete phase diagrams that depend on the primary amino acid sequence. The ability to model these effects from theory can be exploited to interpret experimental observation of the phase behavior of real IDPs or to design further experiments to understand the thermodynamic driving forces of coacervation in biological polymers.

## Supplementary Material

Refer to Web version on PubMed Central for supplementary material.

## ACKNOWLEDGMENTS

This research is supported by the National Institutes of Health (NIH) under Grant Number R01AG05605 and by the MRSEC Program of the National Science Foundation under Award No. DMR 1720256. The authors also acknowledge support from the National Science Foundation NSF under Award No. MCB-1716956. This research used resources of the Extreme Science and Engineering Discovery Environment (XSEDE, supported by the NSF Project TG-MCA05S027) and the Center for Scientific Computing from the California NanoSystems Institute UC Santa Barbara (CNSI) available through the Materials Research Laboratory (MRL): an NSF MRSEC (DMR-1720256) and NSF CNS-1725797.

## REFERENCES

- (1). Dyson HJ; Wright PE Intrinsically Unstructured Proteins and Their Functions. *Nat. Rev. Mol. Cell Biol* 2005, 6, 197–208. [PubMed: 15738986]
- (2). Uversky VN; Gillespie JR; Fink AL Why Are “Natively Unfolded” Proteins Unstructured under Physiologic Conditions? *Proteins: Struct., Funct., Genet* 2000, 41, 415–427. [PubMed: 11025552]
- (3). Forman-Kay JD; Mittag T From Sequence and Forces to Structure, Function, and Evolution of Intrinsically Disordered Proteins. *Structure* 2013, 21, 1492–1499. [PubMed: 24010708]
- (4). Riek R; Eisenberg DS The Activities of Amyloids from a Structural Perspective. *Nature* 2016, 539, 227–235. [PubMed: 27830791]
- (5). Chiti F; Dobson CM Protein Misfolding, Functional Amyloid, and Human Disease. *Annu. Rev. Biochem* 2006, 75, 333–366. [PubMed: 16756495]
- (6). Brangwynne CP; Eckmann CR; Courson DS; Rybarska A; Hoege C; Gharakhani J; Ilicher F; Hyman AA. Germline P Granules are Liquid Droplets that Localize by Controlled Dissolution/Condensation. *Science* 2009, 324, 1729–1732. [PubMed: 19460965]

- (7). Uversky VN; Kuznetsova IM; Turoverov KK; Zaslavsky B Intrinsically Disordered Proteins as Crucial Constituents of Cellular Aqueous Two Phase Systems and Coacervates. *FEBS Lett* 2015, 589, 15–22. [PubMed: 25436423]
- (8). Patel A; Lee HO; Jawerth L; Maharana S; Jahnel M; Hein MY; Stoykov S; Mahamid J; Saha S; Franzmann TM; et al. A Liquid-to-solid Phase Transition of the ALS Protein FUS Accelerated by Disease Mutation. *Cell* 2015, 162, 1066–1077. [PubMed: 26317470]
- (9). Molliex A; Temirov J; Lee J; Coughlin M; Kanagaraj AP; Kim HJ; Mittag T; Taylor JP Phase Separation by Low Complexity Domains Promotes Stress Granule Assembly and Drives Pathological Fibrillization. *Cell* 2015, 163, 123–133. [PubMed: 26406374]
- (10). Zhang X; Lin Y; Eschmann NA; Zhou H; Rauch JN; Hernandez I; Guzman E; Kosik KS; Han S RNA Stores Tau Reversibly in Complex Coacervates. *PLoS Biol* 2017, 15, No. e2002183. [PubMed: 28683104]
- (11). Nott TJ; Petsalaki E; Farber P; Jervis D; Fussner E; Plochowietz A; Craggs TD; Bazett-Jones DP; Pawson T; Forman-Kay JD; et al. Phase Transition of a Disordered Nuage Protein Generates Environmentally Responsive Membraneless Organelles. *Mol. Cell* 2015, 57, 936–947. [PubMed: 25747659]
- (12). Ambadipudi S; Biernat J; Riedel D; Mandelkow E; Zweckstetter M Liquid–liquid Phase Separation of the Microtubule-binding Repeats of the Alzheimer-related Protein Tau. *Nat. Commun* 2017, 8, 275. [PubMed: 28819146]
- (13). Wegmann S; Eftekharzadeh B; Tepper K; Zoltowska KM; Bennett RE; Dujardin S; Laskowski PR; MacKenzie D; Kamath T; Commins C; et al. Tau Protein Liquid–liquid Phase Separation Can Initiate Tau Aggregation. *EMBO J* 2018, 37, No. e98049. [PubMed: 29472250]
- (14). Ferreon JC; Jain A; Choi K-J; Tsoi PS; MacKenzie KR; Jung SY; Ferreon AC Acetylation Disfavors Tau Phase Separation. *Int. J. Mol. Sci* 2018, 19, 1360.
- (15). Brangwynne CP; Mitchison TJ; Hyman AA Active Liquid-like Behavior of Nucleoli Determines Their Size and Shape in *Xenopus laevis* Oocytes. *Proc. Natl. Acad. Sci. U. S. A* 2011, 108, 4334–4339. [PubMed: 21368180]
- (16). Itakura AK; Futia RA; Jarosz DF It pays to be in phase. *Biochemistry* 2018, 57, 2520–2529. [PubMed: 29509425]
- (17). Lin Y-H; Forman-Kay JD; Chan HS Theories for Sequence-Dependent Phase Behaviors of Biomolecular Condensates. *Biochemistry* 2018, 57, 2499–2508. [PubMed: 29509422]
- (18). Overbeek JTG; Voorn M Phase Separation in Polyelectrolyte Solutions. *Theory of Complex Coacervation. J. Cell. Comp. Physiol* 1957, 49, 7–26.
- (19). Veis A; Aranyi C Phase Separation in Polyelectrolyte Systems. I. Complex Coacervates of Gelatin. *J. Phys. Chem* 1960, 64, 1203–1210.
- (20). Delaney KT; Fredrickson GH Theory of Polyelectrolyte Complexation: Complex Coacervates are Self-coacervates. *J. Chem. Phys* 2017, 146, 224902. [PubMed: 29166038]
- (21). Lin Y-H; Forman-Kay JD; Chan HS Sequence-specific Polyampholyte Phase Separation in Membraneless Organelles. *Phys. Rev. Lett* 2016, 117, 178101. [PubMed: 27824447]
- (22). Lin Y-H; Song J; Forman-Kay JD; Chan HS Random-phase-approximation Theory for Sequence-dependent, Biologically Functional Liquid-liquid Phase Separation of Intrinsically Disordered Proteins. *J. Mol. Liq* 2017, 228, 176–193.
- (23). Gonza ez-Mozuelos P; De La Cruz MO Random Phase Approximation for Complex Charged Systems: Application to Copolyelectrolytes (Polyampholytes). *J. Chem. Phys* 1994, 100, 507–517.
- (24). Lin Y-H; Chan HS Phase Separation and Single-chain Compactness of Charged Disordered Proteins are Strongly Correlated. *Biophys. J* 2017, 112, 2043–2046. [PubMed: 28483149]
- (25). Fredrickson G *The Equilibrium Theory of Inhomogeneous Polymers*; Oxford University Press: Oxford, U.K., 2006.
- (26). Das S; Eisen A; Lin Y-H; Chan HS A Lattice Model of Charge-pattern-dependent Polyampholyte Phase Separation. *J. Phys. Chem. B* 2018, 122, 5418–5431. [PubMed: 29397728]
- (27). Shen K; Wang Z-G Electrostatic Correlations and the Polyelectrolyte Self Energy. *J. Chem. Phys* 2017, 146, 084901. [PubMed: 28249457]

- (28). Shen K; Wang Z-G Polyelectrolyte Chain Structure and Solution Phase Behavior. *Macromolecules* 2018, 51, 1706–1717.
- (29). Lytle TK; Sing CE Transfer Matrix Theory of Polymer Complex Coacervation. *Soft Matter* 2017, 13, 7001–7012. [PubMed: 28840212]
- (30). Radhakrishna M; Basu K; Liu Y; Shamsi R; Perry SL; Sing CE Molecular Connectivity and Correlation Effects on Polymer Coacervation. *Macromolecules* 2017, 50, 3030–3037.
- (31). Chang L-W; Lytle TK; Radhakrishna M; Madinya JJ; Ve ez J; Sing CE; Perry SL Sequence and Entropy-based Control of Complex Coacervates. *Nat. Commun* 2017, 8, 1273. [PubMed: 29097695]
- (32). Das S; Amin AN; Lin Y-H; Chan HS Coarse-grained Residue-based Models of Disordered Protein Condensates: Utility and Limitations of Simple Charge Pattern Parameters. *Phys. Chem. Chem. Phys* 2018, 20, 28558–28574. [PubMed: 30397688]
- (33). Blas FJ; MacDowell LG; de Miguel E; Jackson G Vapor-liquid Interfacial Properties of Fully Flexible Lennard-Jones Chains. *J. Chem. Phys* 2008, 129, 144703. [PubMed: 19045161]
- (34). Silmore KS; Howard MP; Panagiotopoulos AZ Vapour-liquid Phase Equilibrium and Surface Tension of Fully Flexible Lennard-Jones Chains. *Mol. Phys* 2017, 115, 320–327.
- (35). Dignon GL; Zheng W; Kim YC; Best RB; Mittal J Sequence Determinants of Protein Phase Behavior from a Coarse-grained Model. *PLoS Comput. Biol* 2018, 14, No. e1005941. [PubMed: 29364893]
- (36). Fredrickson GH; Ganesan V; Drolet F Field-theoretic Computer Simulation Methods for Polymers and Complex Fluids. *Macromolecules* 2002, 35, 16–39.
- (37). Ganesan V; Fredrickson G Field-theoretic Polymer Simulations. *Europhys. Lett* 2001, 55, 814.
- (38). Lee J; Popov YO; Fredrickson GH Complex Coacervation: A Field Theoretic Simulation Study of Polyelectrolyte Complexation. *J. Chem. Phys* 2008, 128, 224908. [PubMed: 18554054]
- (39). Popov YO; Lee J; Fredrickson GH Field-theoretic Simulations of Polyelectrolyte Complexation. *J. Polym. Sci., Part B: Polym. Phys* 2007, 45, 3223–3230.
- (40). Riggleman RA; Kumar R; Fredrickson GH Investigation of the Interfacial Tension of Complex Coacervates Using Field-theoretic Simulations. *J. Chem. Phys* 2012, 136, 024903. [PubMed: 22260612]
- (41). Das RK; Pappu RV Conformations of Intrinsically Disordered Proteins are Influenced by Linear Sequence Distributions of Oppositely Charged Residues. *Proc. Natl. Acad. Sci. U. S. A* 2013, 110, 13392–13397. [PubMed: 23901099]
- (42). Danielsen SPO; McCarty J; Shea J-E; Delaney KT; Fredrickson GH Molecular Design of Self-Coacervation Phenomena in Block Polyampholytes. *Proc. Natl. Acad. Sci. U.S.A* 2019, DOI: 10.1073/pnas.1900435116.
- (43). Sawle L; Ghosh K A Theoretical Method to Compute Sequence Dependent Configurational Properties in Charged Polymers and Proteins. *J. Chem. Phys* 2015, 143, 085101. [PubMed: 26328871]
- (44). Doi M; Edwards SF *The Theory of Polymer Dynamics*; Oxford University Press: Oxford, U.K., 1988.
- (45). Firman T; Ghosh K Sequence Charge Decoration Dictates Coil-globule Transition in Intrinsically Disordered Proteins. *J. Chem. Phys* 2018, 148, 123305. [PubMed: 29604827]
- (46). Delaney KT; Fredrickson GH Recent Developments in Fully Fluctuating Field-theoretic Simulations of Polymer Melts and Solutions. *J. Phys. Chem. B* 2016, 120, 7615–7634. [PubMed: 27414265]
- (47). Coslovich D; Hansen J-P; Kahl G Ultrasoft Primitive Model of Polyionic Solutions: Structure, Aggregation, and Dynamics. *J. Chem. Phys* 2011, 134, 244514. [PubMed: 21721650]
- (48). Warren PB; Vlasov A; Anton L; Masters AJ Screening Properties of Gaussian Electrolyte Models, with Application to Dissipative Particle Dynamics. *J. Chem. Phys* 2013, 138, 204907. [PubMed: 23742516]
- (49). Plimpton S Fast Parallel Algorithms for Short-range Molecular Dynamics. *J. Comput. Phys* 1995, 117, 1–19.

- (50). Riggleman RA; Fredrickson GH Field-theoretic Simulations in the Gibbs Ensemble. *J. Chem. Phys* 2010, 132, 024104. [PubMed: 20095660]
- (51). Mester Z; Lynd NA; Fredrickson GH Numerical Self-consistent Field Theory of Multicomponent Polymer Blends in the Gibbs Ensemble. *Soft Matter* 2013, 9, 11288–11294.
- (52). Higgs PG; Joanny J-F Theory of Polyampholyte Solutions. *J. Chem. Phys* 1991, 94, 1543–1554.
- (53). Ha B-Y; Thirumalai D Conformations of a Polyelectrolyte Chain. *Phys. Rev. A: At., Mol., Opt. Phys* 1992, 46, R3012.
- (54). Samanta HS; Chakraborty D; Thirumalai D Charge Fluctuation Effects on the Shape of Flexible Polyampholytes with Applications to Intrinsically Disordered Proteins. *J. Chem. Phys* 2018, 149, 163323. [PubMed: 30384718]
- (55). Pappu RV; Wang X; Vitalis A; Crick SL A Polymer Physics Perspective on Driving Forces and Mechanisms for Protein Aggregation. *Arch. Biochem. Biophys* 2008, 469, 132–141. [PubMed: 17931593]
- (56). Müller-Späth S; Soranno A; Hirschfeld V; Hofmann H; Ruegger S; Reymond L; Nettels D; Schuler B Charge Interactions Can Dominate the Dimensions of Intrinsically Disordered Proteins. *Proc. Natl. Acad. Sci. U. S. A* 2010, 107, 14609–14614. [PubMed: 20639465]
- (57). Dignon GL; Zheng W; Best RB; Kim YC; Mittal J Relation Between Single-molecule Properties and Phase Behavior of Intrinsically Disordered Proteins. *Proc. Natl. Acad. Sci. U. S. A* 2018, 115, 9929–9934. [PubMed: 30217894]
- (58). Perry SL; Sing CE Prism-based Theory of Complex Coacervation: Excluded Volume versus Chain Correlation. *Macromolecules* 2015, 48, 5040–5053.
- (59). Danielsen SPO; McCarty J; Shea J-E; Delaney KT; Fredrickson GH Small Ion Effects on Self-Coacervation Phenomena in Block Polyampholytes 2019, manuscript in preparation.
- (60). Brady JP; Farber PJ; Sekhar A; Lin Y-H; Huang R; Bah A; Nott TJ; Chan HS; Baldwin AJ; Forman-Kay JD; et al. Structural and Hydrodynamic Properties of an Intrinsically Disordered Region of a Germ Cell-specific Protein on Phase Separation. *Proc. Natl. Acad. Sci. U. S. A* 2017, 114, E8194–E8203. [PubMed: 28894006]

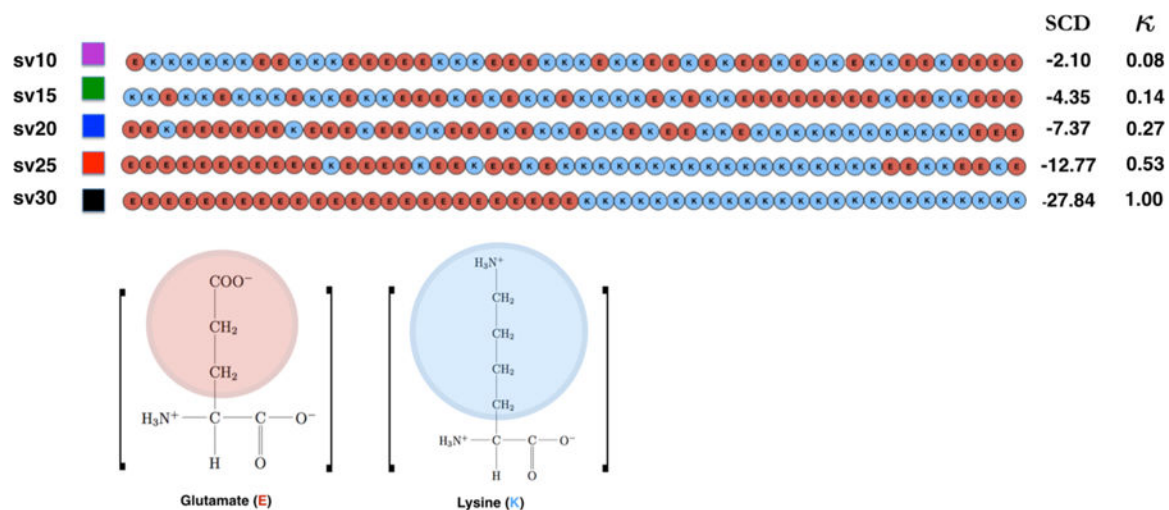


**Figure 1.** Five model IDP sequences of glutamate and lysine considered in this work. Sequences and nomenclature were originally introduced in ref 41. Also shown are the sequence charge decoration (SCD) metric of Sawle and Ghosh<sup>43</sup> and the  $\kappa$  parameter of Das and Pappu<sup>41</sup>

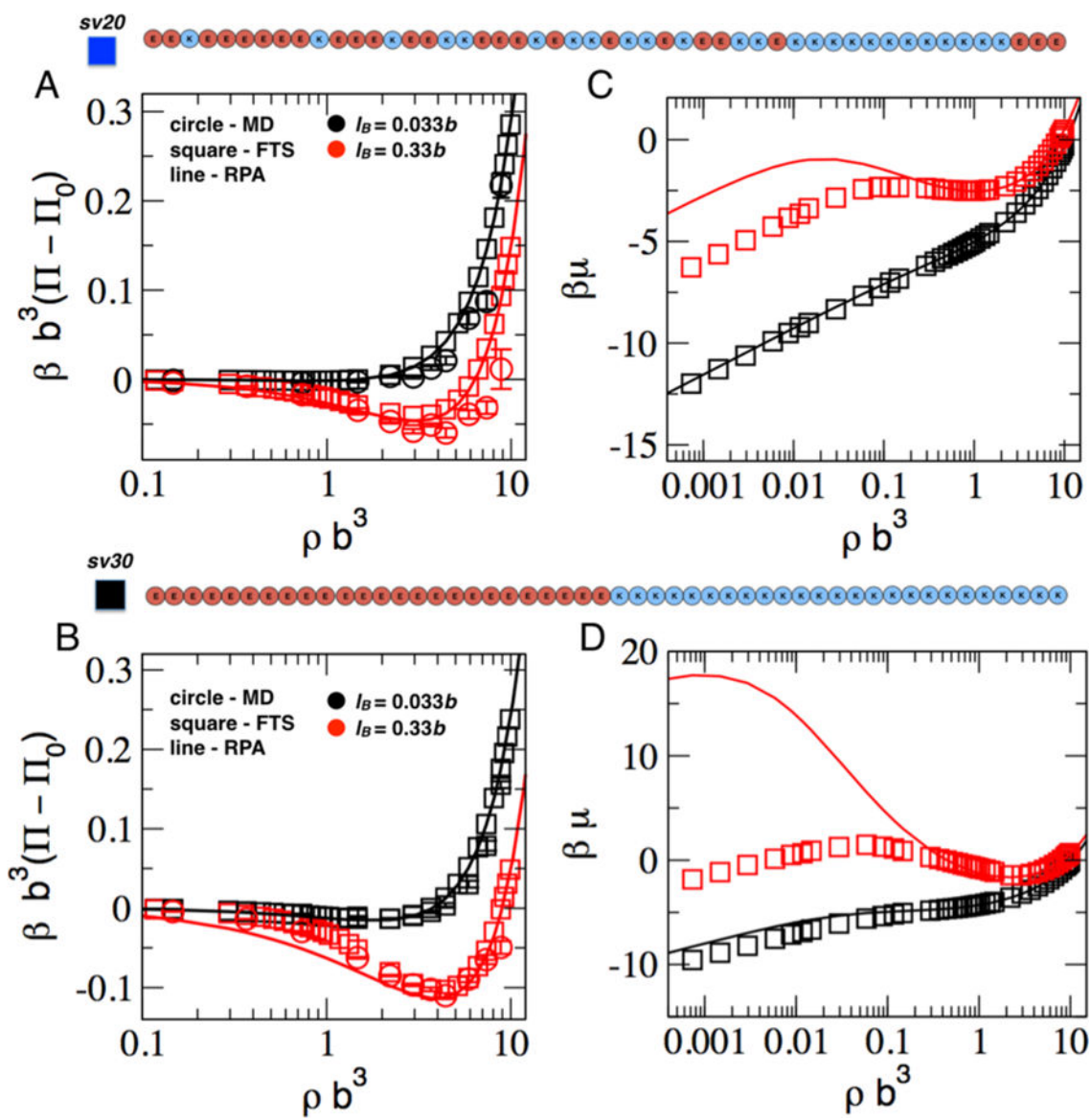


**Figure 2.**

Left column: Excess osmotic pressure evaluated from particle MD (open circle), FTS (open square), and RPA (solid line) for model sequences *sv20* (A) and *sv30* (B) as a function of monomer density. Simulations were performed using a Bjerrum length of  $l_B = 0.033b$  (black) and  $l_B = 0.33b$  (red). Right column: Chemical potential as a function of monomer density for *sv20* (C) and *sv30* (D) with Bjerrum length  $l_B = 0.033b$  (black) and  $l_B = 0.33b$  (red). FTS results are represented with open squares, and the solid line depicts the RPA expression.

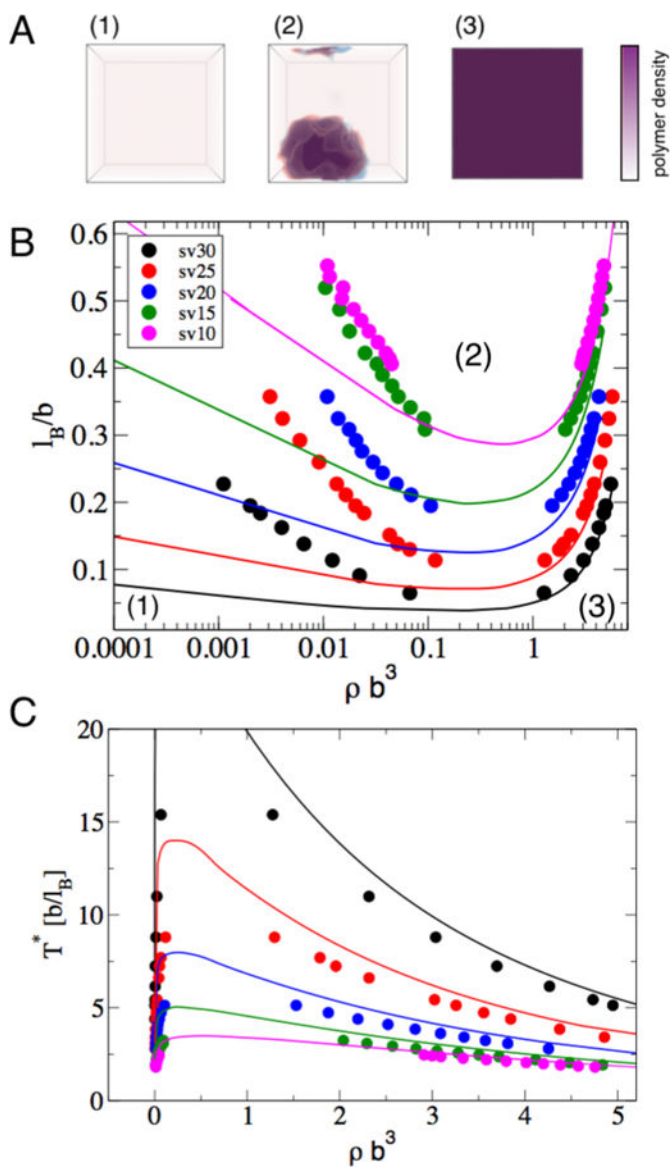


**Figure 3.** (A) Snapshot of the polymer density profiles from FTS for three regions of the phase diagram: (1) a dilute solution phase; (2) a two-phase region in which a dilute supernatant and dense coacervate phase coexist; and (3) a dense protein region. (B) Coexistence curves evaluated from FTS using the Gibbs ensemble (points) and computed from RPA (solid lines). The coloring scheme is the same as that in Figure 1, representing the five different chain sequences, showing a strong charge sequence dependence on the two phase window. (C) Coexistence curves showing the reduced temperature vs monomer density. The linear scale of the horizontal axis highlights the features of the dense branch of the phase diagram but conceals the dilute branch. All simulations were performed without explicit counterions present.



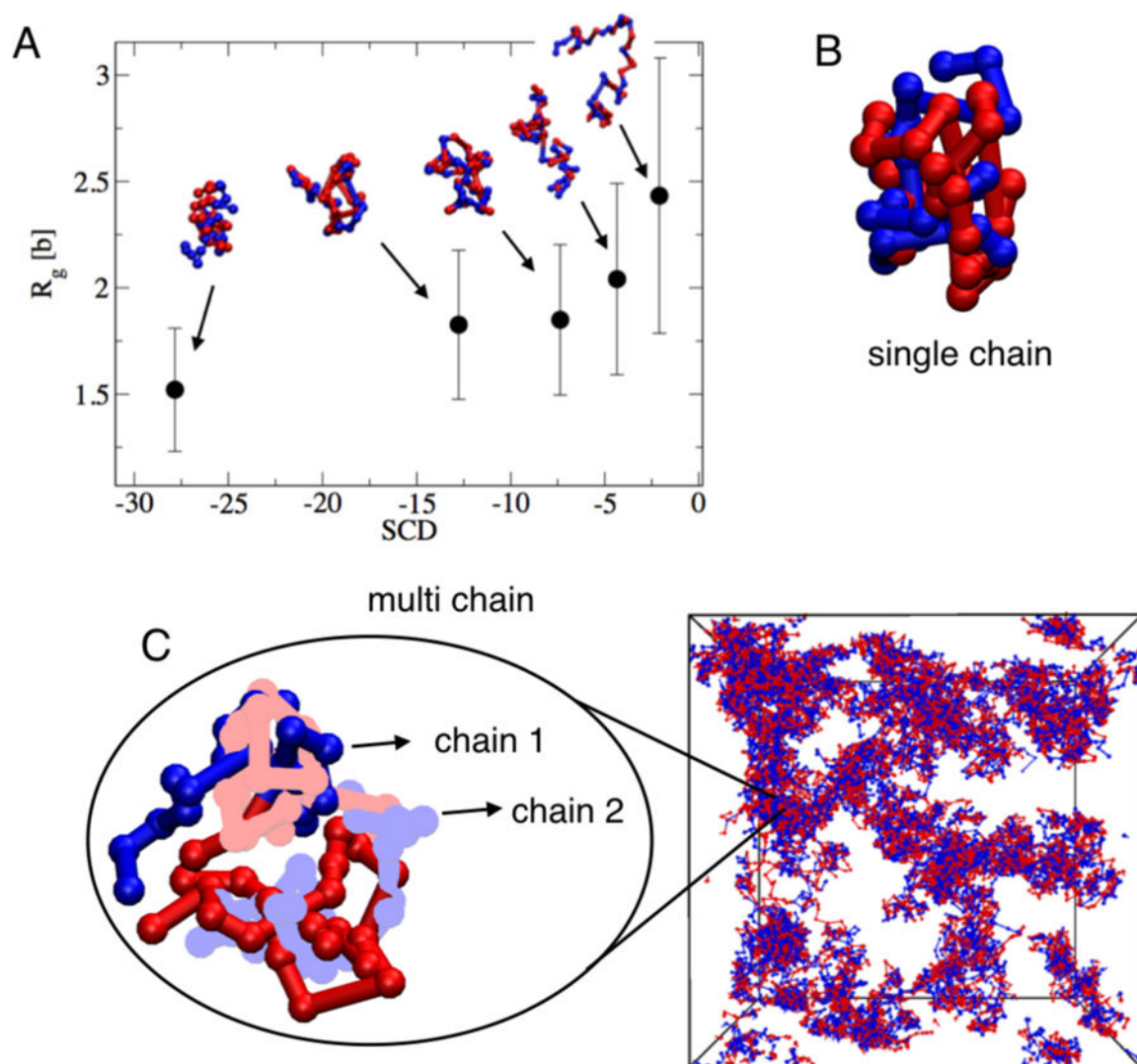


**Figure 4.**

(A) Average radius of gyration for each of the five sequences evaluated from a single-chain particle MD simulation. The horizontal axis is the SCD metric of Sawle and Ghosh.<sup>43</sup> A representative chain configuration for each sequence is also shown. All single-chain simulations we performed at  $l_B = 0.33b$  without explicit counterions present. (B) Representative configuration from a single-chain particle MD simulation showing intramolecular association between oppositely charged “patches” for the diblock chain *sv30*. (C) Snapshot of two representative chains from a particle MD simulation of 300 chains showing early stages of aggregation due to intermolecular association between oppositely charged groups. Chain 1 is opaque and chain 2 is shaded for contrast.

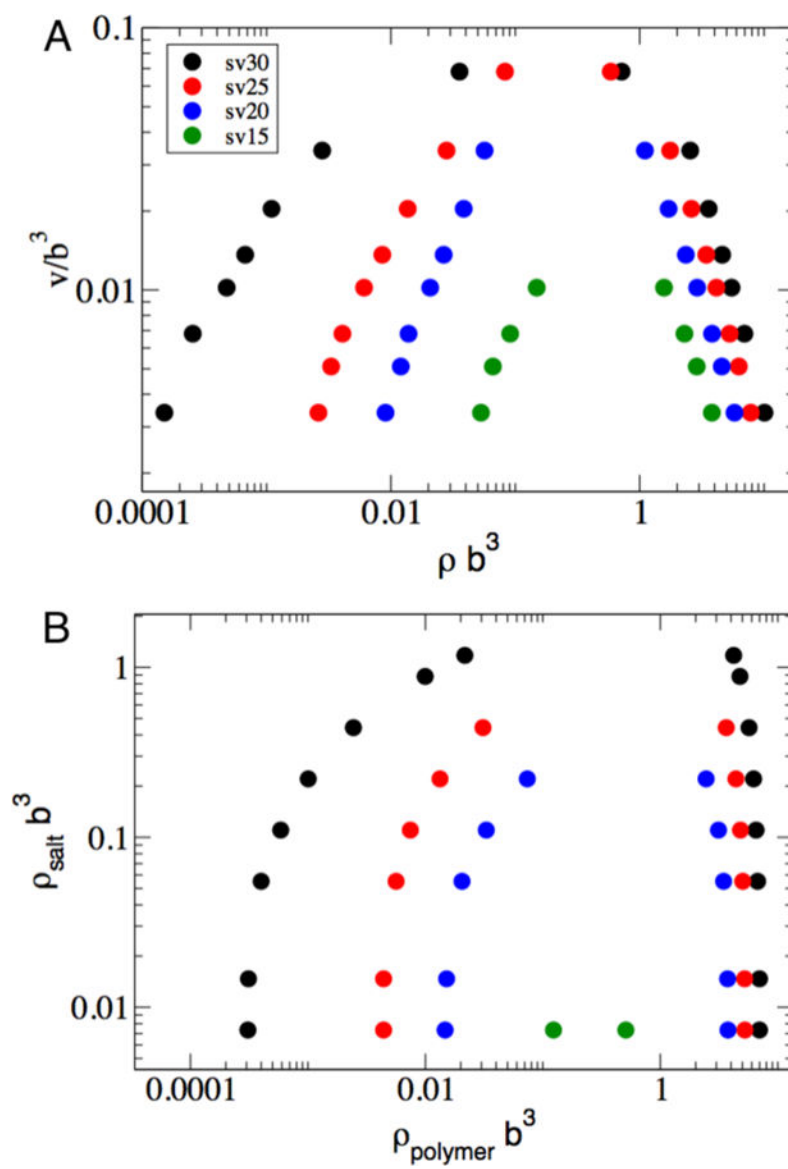


**Figure 5.**

(A) Coexistence points evaluated from FTS using the Gibbs ensemble at fixed  $l_B = 0.33b$  with varying excluded volume strength. Simulations were performed without explicit counterions present. The coloring scheme is the same as that in Figure 1, representing four different chain sequences. (B) Coexistence points evaluated at fixed  $v = 0.0069b^3$  and  $l_B = 0.33b$  at varying salt concentration by introducing explicit salt ions as point particles into the polymer model.